2021

The Performance of an Automotive Carbon Dioxide Heat Pump System in Frosting and Defrosting

Wenying Zhang
University of Illinois Urbana-Champaign, wenying3@illinois.edu

Pega Hrnjak
University of Illinois Urbana-Champaign

The Performance of an Automotive Carbon Dioxide Heat Pump System in Frosting and Defrosting

Wenying ZHANG [1], Pega HRNJAK [2]*

[1]ACRC, University of Illinois, Urbana, Illinois, USA
wenying3@illinois.edu

[2]Creative Thermal Solutions, Inc., Urbana, Illinois, USA
pega@illinois.edu

* Corresponding Author

ABSTRACT

This paper presents the performance in frosting and defrosting of an automotive carbon dioxide (CO_2) heat pump system, which is composed of a microchannel indoor and outdoor coil, a reciprocating compressor, an electronic expansion valve, and an integrated accumulator and internal heat exchanger. The effects of the criterion for the start of defrosting on the heat pump system performance were investigated experimentally. The defrost-start criterion was determined based on the reduction in the performance of the heat pump system instead of only considering the performance of the outdoor coil. Results show the heat pump system can operate for 64 minutes at 0℃ and 90% RH with a defrost-start criterion of 10 times the initial air-side pressure drop. The accumulator and internal heat exchanger improve system efficiency during frosting conditions. The mass of frost accumulation increases faster in the first 40 minutes and slower in the next 24 minutes for 0℃ and 90% RH. The retained water on the outdoor coil gets saturated after three short frosting/ defrosting cycles or a 64-minute long run. Also, the frosting and defrosting processes are monitored by a web camera to investigate the frost distribution on the two-pass outdoor microchannel heat exchanger. The results are presented for evaluating the frosting distribution and the effects on the overall performance of the heat pump system.

1. INTRODUCTION

In recent decades, electric vehicles have gotten more attention in the automotive industry. However, it faces the challenge of range anxiety, especially in low temperatures. The energy density of the battery reduces, and the cabin requires more thermal energy to keep passengers warm. Heat pumps are more efficient than electric heaters to provide heating capacity, but there are still concerns related to frosting/ defrosting issues, condensate removal, and drainage.

In the earlier stage, researchers focused more on the fundamental aspects, like the mechanism of frost growth and frost properties. Hayashi et al. (1977) classified the frost formation types based on the structure in the temperature range of 0 to -25℃. The density and effective thermal conductivity were studied and related to the frost formation types. Robinson and Jacobi (2001) investigated the leading-edge and trailing-edge effects on frost formation and extended existing models to predict frost thickness, density, and interface temperature for a fin under different conditions.

Later, there were studies of surface treatment for thermal performance improvement. Rahman and Jacobi (2014) examined the effects of microgroove geometry and water retention on frost growth and properties. The result shows the properties become repeatable from the third frost cycle, and the microgrooves increase the frost thickness but decrease the frost density in all frosting cycles.

For microchannel heat exchangers, which are widely used in automobile air-conditioning systems, there are numerous studies related to the effects of geometries and sequential frosting. Xia et al. (2006) explored the thermal-

hydraulic behavior of microchannel heat exchangers with louver fin under conditions of air-side frosting, defrosting, and re-frosting using coolant. They also developed a numerical model to predict the transient performance of the HX, and it predicts the heat transfer performance well. Zhang and Hrnjak (2010) studied the hydraulic performance, frost accumulation, and water retention of a parallel flow parallel fin HX in periodic frosting using precooled/preheated ethyl alcohol. The results show it takes a few cycles of periodic frosting to come to repeatable conditions. The effects of a fan, relative humidity, and different orientations were compared.

Recently, there have been some simulation papers and review papers discussing the frosting and defrosting of heat exchangers of heat pumps in electric vehicles. Steiner and Rieberer (2013) built a transient model for a reversible CO_2 HP system using Modelica. They validated the model with experimental data and studied the effects of EXV opening on defrosting efficiency and time.

However, those researchers focus on the performance of heat exchangers only, while this paper presents a study of the frosting/defrosting performance with a full CO_2 HP system. For example, some review papers are using data for frosting on tube and fin heat exchangers, and some are applying conditions of residential systems. For instance, air face velocity is lower than 1.5 m/s, and air inlet temperature is higher than 10°C in some research papers. However, for the CO_2 HP system in this paper, the temperature difference between air and the evaporating temperature is close to 2 or 3°C when the outdoor air velocity is 3.0 m/s. Therefore, there is no frosting issue when the outdoor air temperature is higher than 3°C for our CO_2 HP system.

2. EXPERIMENTAL SETUP

2.1 Facility

Figure 1 and Figure 2 show the schematic of the reversible CO_2 air-conditioning system in both AC/ defrost and HP modes. The dimensions of the key components are listed in Table 1. The performances of the HP system during frosting and defrosting conditions were experimentally studied within two climate chambers: outdoor and indoor chambers. Each climate chamber is composed of a wind tunnel with VFD controlled blower, a PID-controlled electric heater, a glycol chiller, a steam line, and related sensors for temperature, pressure, and humidity measurements. The detailed measurement points for both air- and refrigerant-side are shown in Figure 1 and Figure 2. Also, the uncertainties of the measurements are listed in Table 2. Besides, the semi-hermetic compressor, mass flow meter, and the integrated IHX/Acc are installed between the two climate chambers. The details of the integrated IHX/Acc can be found in our previous work (Zhang and Hrnjak, 2020).

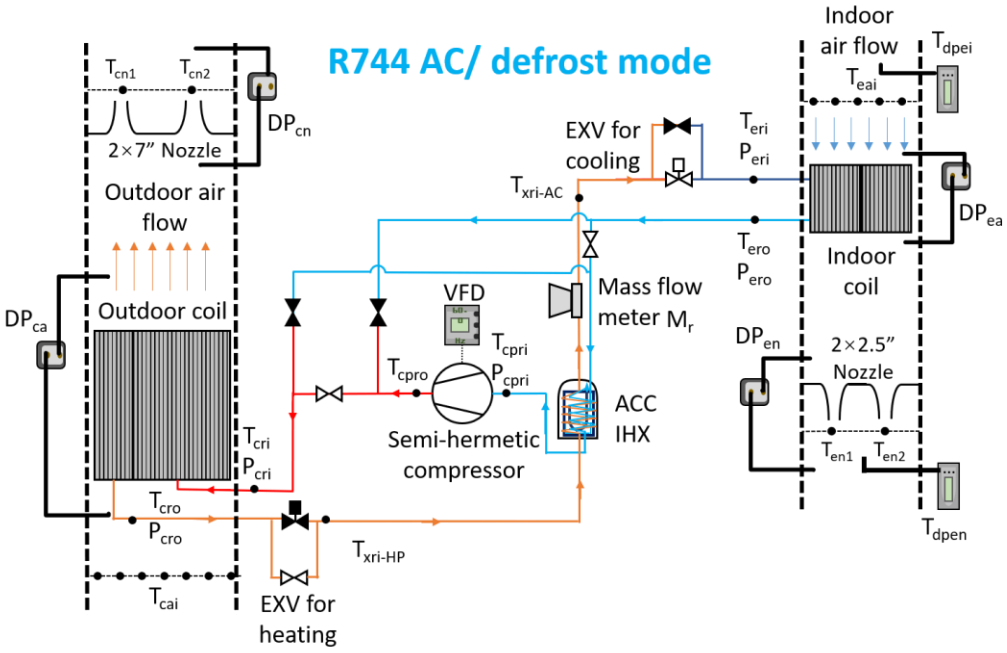

Figure 1: Schematic drawing of the CO2 system in AC/ defrost mode

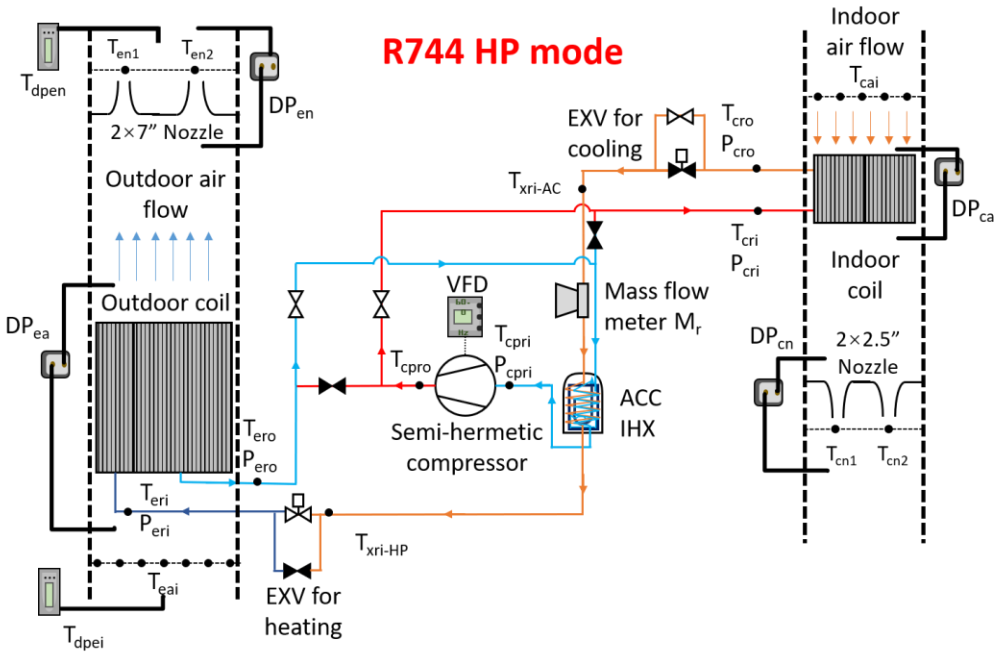

Figure 2: Schematic drawing of the CO2 system in HP mode

The outdoor coil is a vertically installed 2-pass microchannel heat exchanger with louver fins. This heat exchanger is designed as a gas cooler for AC mode, and the performance as an outdoor evaporator in frost conditions is analyzed in the following chapter.

Table 1: Dimensions of key components

Component	Dimensions
Outdoor coil (1-slab, 2-pass: 17/ 34 tubes)	• Overall dimension (mm): 635 (H) × 467 (W) × 16 (T) • Fin height (mm): 8.0 • Fin pitch (mm): 1.3 • Fin thickness (mm): 0.1 • Louver length (mm): 7.2 • Louver pitch (mm): 0.9
Indoor coil (2-slab, 4- pass: all 17 tubes)	• Overall dimension (mm): 229 (H) × 248 (W) × 35 (T) • Fin height (mm): 5.6 • Fin pitch (mm): 1.4 • Fin thickness (mm): 0.08 • Louver length (mm): 4.9 • Louver pitch (mm): 1.12
Internal heat exchanger/ Accumulator	• Overall dimension (mm): 247 (H) × 85 (D) • Counter-flow IHX for AC/ defrost mode • Parallel-flow IHX for HP mode • Nylon accumulator
Semi-hermetic reciprocating compressor	• 2-cylinder • Displacement: 2.39 m^3/h (50 Hz), 2.87 m^3/h (60 Hz) • 1450 rpm @ 50 Hz, 1750 rpm @ 60 Hz • 3.8 HP, 208~ 230V/ 3/ 60 Hz
Electronic expansion valve	• Actuator step range: 2500

Table 2: Uncertainties of air- and refrigerant-side instruments

Parameter	Sensor	Range	Uncertainty
Refrigerant temperature [℃]	T-type thermocouple	-50 to 150	± 0.2
Refrigerant low-side pressure [psi]	Strain gage	0 to 1000	± 0.5
Refrigerant high-side pressure [psi]	Strain gage	0 to 3000	± 1.5
Refrigerant/ glycol mass flow rate [kg/h]	Coriolis-type	0 to 2180/ 0 to 6800	± 0.10% of reading
Electrical power of compressor [kW]	3-phase wattmeter	0 to 6	± 0.20% of reading
Condensate weight [g]	Strain Gauge	0 to 800	± 0.10% of full scale
Air temperature [℃]	T-type welded thermocouple	-50 to 150	± 0.2
Dew point temperature [℃]	Chilled mirror dew point sensor	-80 to 85	± 0.2
Pressure drop of air-side [Pa]	Differential pressure transducer	0 to 600	± 0.25% of full scale

2.2 Experimental procedures and data reduction

The performances of the CO_2 HP system in periodic frosting and defrosting conditions are studied with several steps of experiments: frosting, defrosting by reversing the system, water collection, and repeat for periodic performances. The operating conditions of the experiments are listed in Table 3.

During the frosting procedure, we first preconditioned the chambers using the HP system, the glycol loop, and the electric heater. To keep the outdoor coil clean, we switched on the glycol loop first and monitored the dew point in the outdoor climate chamber until it reached -5℃. Then, we turned on the HP system and controlled the compressor speed and EXV opening to make sure the evaporating temperature was higher than the dew point. After outdoor and indoor air inlet temperatures T_{eai} and T_{cai} reached the target values, steam was added into the outdoor chamber until it was the desired relative humidity RH_{ei} and kept constant. Then, we started recording the data and frost distribution images at an interval of 6 s until the pressure drop across the outdoor coil reached the criterion of starting defrost. During this procedure, the blower speeds were fixed to provide the air velocity $V_{eai,ini}$, and U_{cai}, which were measured by ASHARE standard nozzles. As frost accumulated on the outdoor coil, the outdoor air velocity V_{eai} could drop to about 1 m/s when the final DP_{ea} reached 10 times the initial DP_{ea}. Also, the compressor speed (1450 rpm) was controlled by VFD at 50 Hz, and the discharge pressure of compressor P_{dis} was controlled by EXV to a value as close to the optimized pressure as possible with the limitation that discharge temperature $T_{r,dis}$ is lower than 140℃. The mass of the frost accumulated on the outdoor coil was determined by integrating the product of humidity difference in front of and behind the outdoor coil and the dry air mass flow rate, as equation (1):

$$M_{frost} = \int_0^t \dot{m}_{outdoor,dryair}(\omega_{eai} - \omega_{eao})dt \quad (1)$$

Where the mass flow rate of the outdoor dry air $m_{outdoor,\ dryair}$ was determined from measured air temperature, dew point, and pressure drop at the outdoor nozzles. The humidity ratios ω_{eai} and ω_{eao} were determined using air temperatures and dew points at outdoor coil inlet and nozzles, individually.

The capacity of the outdoor evaporator in HP mode was calculated based on the average data of every 2 minutes using equation (2):

$$Q_{e,air} = \dot{m}_{outdoor,dryair}(h_{eai} - h_{eao}) \quad (2)$$

Where the enthalpies of air h_{eai} and h_{eao} were determined using air temperatures and dew points at outdoor coil inlet and nozzles. The capacity of the indoor gas cooler, however, was calculated in three different approaches: air- and refrigerant-side, as equation (3) to (4):

$$Q_{c,air} = \dot{m}_{indoor,dryair}(h_{cao} - h_{cai}) \tag{3}$$

$$Q_{c,ref} = (1-OCR)\dot{m}_r(h_{cri} - h_{cro}) + OCR \cdot \dot{m}_r(h_{coi} - h_{coo}) \tag{4}$$

Where the indoor air mass flow rate $m_{indoor,dryair}$ was determined from measured air temperature, dew point, and pressure drop at the indoor nozzles. The enthalpies of air h_{cai} and h_{cao} were determined using air temperatures and dew points at the indoor coil inlet and nozzles. For the refrigerant side, *OCR* is the oil circulation ratio, measured by the sampler installed across the mass flow meter on the liquid line. M_r is measured by the mass flow meter and is actually the mass flow rate of oil and CO_2 mixture. Refrigerant enthalpies h_{cri} and h_{cro}, oil enthalpies h_{coi} and h_{coo} are determined from the pressures and temperatures measured at indoor coil inlet and outlet. Besides, the relative uncertainties of heating capacity are 1.3% and 4.0% for refrigerant- and air-side, respectively. It is 5.1% for the air-side cooling capacity.

Similarly, the capacity of the IHX was calculated using the high-pressure refrigerant-side:

$$Q_{IHX,high} = (1-OCR)\dot{m}_r(h_{cro} - h_{xri}) + OCR \cdot \dot{m}_r(h_{coo} - h_{xoi}) \tag{5}$$

Where refrigerant enthalpy h_{xri} and oil enthalpy h_{xoi} are determined from the pressure and temperature measured at the inlet of the expansion valve. Also, the low-pressure side capacity equals the high-pressure side capacity, assuming no heat loss to the ambient.

Table 3: Operating conditions of frosting/defrosting experiments

Microchannel tube orientation	**T_{eai} [°C]**	**RH_{ei} [%]**	**$V_{eai,ini}$ [m/s]**	**T_{cai} [°C]**	**U_{cai} [kg/min]**	**# of frosting cycle**	**Defrost start criterion**	**Defrost stop criterion**
Vertical	0	90	3.0	20	7.0	1/ 2/ 3	5/ 10× $DP_{ea,ini}$	T_{cro} = 45 °C

Then, for the defrost procedure, the HP system was switched off once the DP_{ea} reached the defrost-start criterion. The valves were adjusted, and the system was reversed to AC/ defrost mode. Additionally, the outdoor blower was off, and the indoor air flow rate and air inlet temperature were controlled the same as in the frost condition. Compressor speed was reduced to 1160 rpm and EXV opening is fixed at 50%. The data were recorded every 6 s while the defrosting images were recorded every 2 s until the outdoor coil exit temperature T_{cro} reached 45°C. Then, repeat the frost and defrost procedures for evaluation of periodic performances if necessary.

Finally, to collect the condensate water, we switched off the compressor, heaters, steam line, and blowers. Then, we collected the retained water using compressed air and paper towels and collected drained water using a beaker. The mass of each part of the water was measured and recorded. The difference between the total amount of frost M_{frost} and the sum of retained water and drained water was considered as the part of water evaporated during the defrosting process.

3. RESULTS AND DISCUSSION

In this paper, 0°C and 90% RH is the most concerning condition considering the operating time of the heat pump system. Because the absolute humidity drops significantly as the ambient air temperature T_{eai} reduces from 0 to -10°C, frost accumulates much slower in colder conditions.

3.1 Effects of different defrost-start criteria on system performance

Figure 3 and Figure 4 show the air-side pressure drop, heating capacity, cooling capacity, HPF, and compressor power of the HP system for 0°C and 90% RH with different defrost-start criteria: 5 and 10 times of the initial DP_{ea}. At the end of the first frosting process, the heating capacity drops by 5.3% for 5 times of the initial DP_{ea}, and 35.6% for 10 times of the initial DP_{ea}. Similarly, the capacity of outdoor coil $Q_{cooling}$ drops 53.3% for 5 times the initial

DP_{ea}, and 85.9% for 10 times the initial DP_{ea}. But the operating time increases from 28 minutes to 64 minutes, which is 128.6% longer, as the defrost-start criterion changes from 5 to 10 times of the initial DP_{ea}.

With 5 times the initial DP_{ea} as the defrost-start criterion, the reduction in the capacity and efficiency of the HP system is negligible. This indicates the HP system has the potential to operate for a longer time if we can tolerate a reduced capacity. The advantage is that we will be able to defrost when the passengers are not in the vehicle. For example, after a 60-minute commuting time, defrosting is conducted when the car is in the parking lot or charging center. The effect of defrosting on passenger comfort can be minimized.

Also, by the end of the first frosting process, the efficiency HPF keeps almost constant for 5 times of the initial DP_{ea} and drops by 15.9% for 10 times of the initial DP_{ea}. This relatively small reduction is because compressor power W_{comp} and heating capacity $Q_{heating}$ drop simultaneously. By the end of the first frosting process, W_{comp} drops by 6.5% for 5 times of the initial DP_{ea} and drops by 23.4% for 10 times of the initial DP_{ea}. On the one hand, as frost accumulates on the outdoor coil, the evaporating pressure drops, and the suction pressure P_{cpri} drops as well. Thus, the suction density and mass flow rate of refrigerant m_r drop, so the compressor power drops. On the other hand, the refrigerant migrates from the indoor gas cooler and liquid line to the accumulator during the frosting process, and this mass transfer compensates for the reduced capacity of the outdoor coil. Therefore, the efficiency of the HP system drops slower than capacity in the frosting process.

For the periodic performance, the three continuous frosting processes with 5 times of the initial DPea as the defrost-start criterion are analyzed. Figure 3 shows the air-side pressure drop DP_{ea} at the beginning of each frosting cycle increases slightly from 43.7 to 56.2 Pa. This is due to the presence of retained water on the coil surface after the defrosting processes. Also, there is a start-up stage at the beginning of the second and third frosting processes, and it takes up to 6 minutes for the heating capacity $Q_{heating}$ to reach "steady-state". The HP system can operate 28,28, and 22 minutes for the first, second, and third frosting processes with 5 times of the initial DP_{ea} as the defrost-start criterion. This shows that most of the frost is removed from the coil surface after approximately the first 30 minutes and the effects on the next run are negligible. However, the retained water increases after the second defrosting process, and the operating time is significantly reduced.

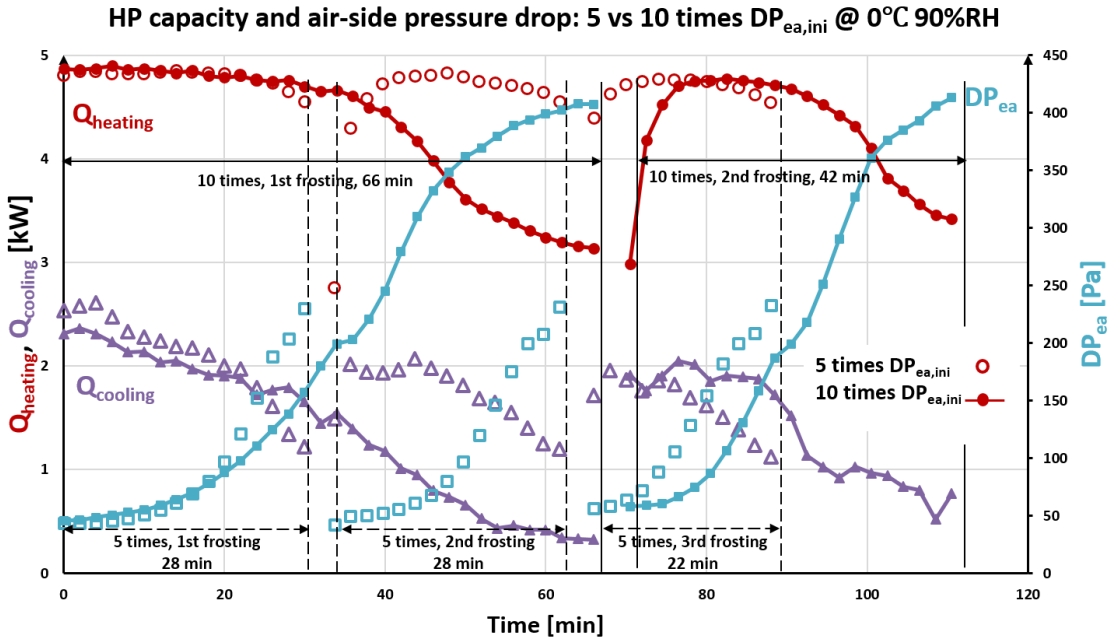

Figure 3: Comparison of $Q_{heating}$, $Q_{cooling}$, and DP_{ea} with different defrost-start criteria for 0°C and 90% RH

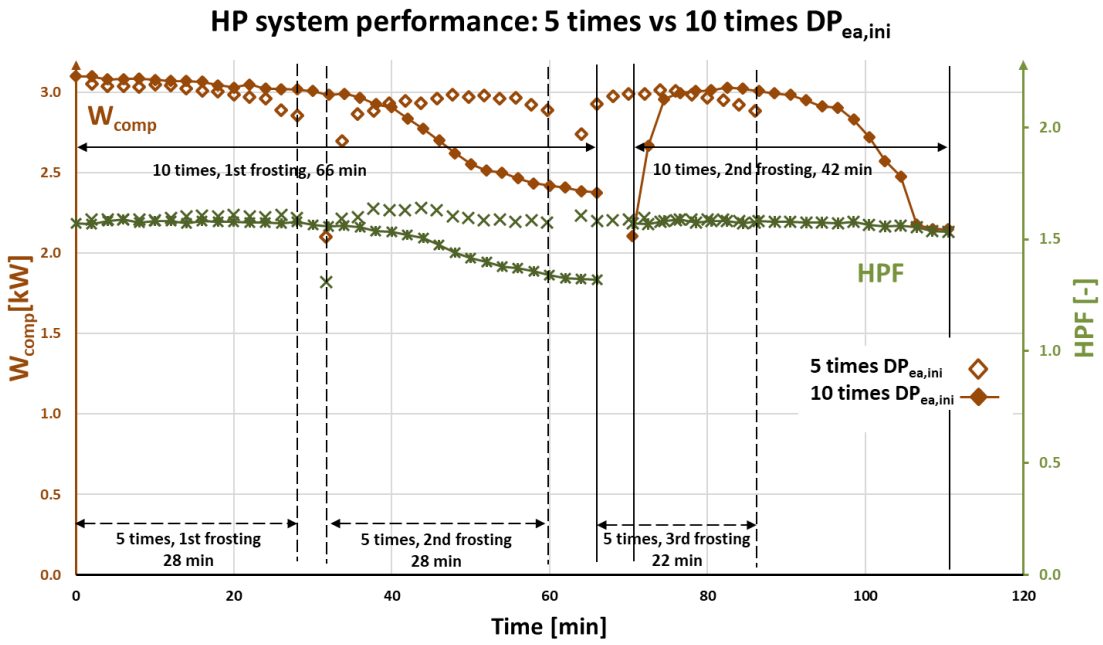

Figure 4: Comparison of HPF and W_{comp} with different defrost-start criteria for 0°C and 90% RH

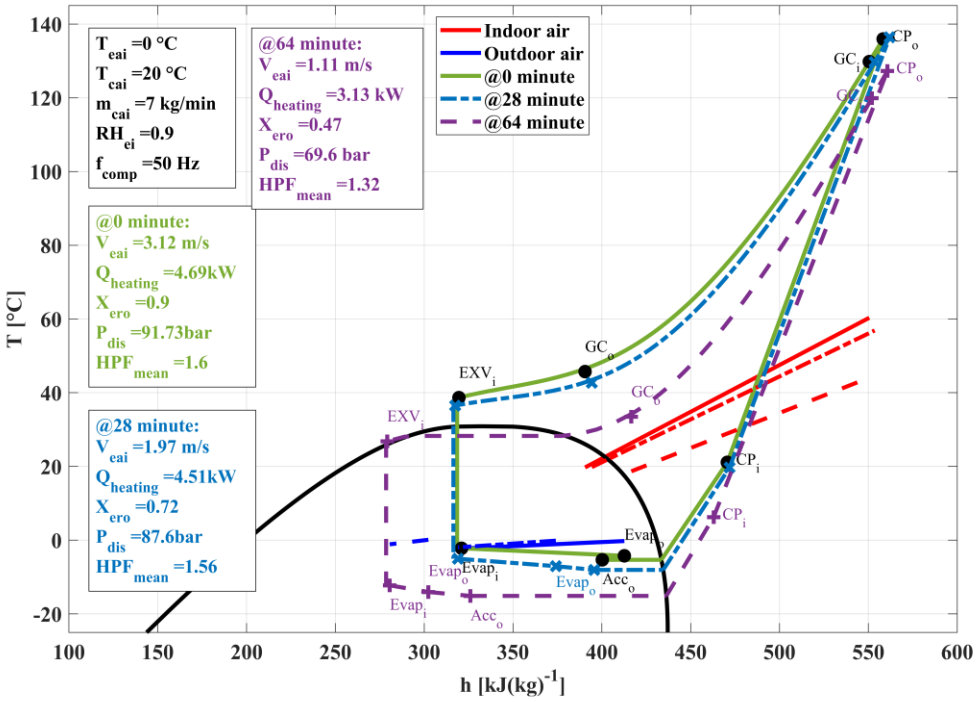

Figure 5: T-h plots of CO_2 HP cycle at 0, 28, and 64 minute of the first frosting process for 0°C 90% RH

Figure 5 illustrates the shift of the T-h plot of the CO_2 HP cycle during the first frosting process for 0°C 90% RH condition. As mentioned earlier, during the first 28 minutes, the reduction of heating capacity and efficiency is minimal. This is due to the existence of the accumulator and the IHX in the HP system. Although the refrigerant quality at the evaporator outlet X_{ero} drops significantly from 0.90 to 0.72, the liquid level in the accumulator increases, and the quality at the accumulator outlet/ IHX inlet $X_{acc,ro}$ varies little, as shown by the green and blue lines in Figure 5. Then, because of the high effectiveness of the IHX, the low-side exit temperature of IHX, which is

the suction temperature of the compressor T_{cpri}, stays the same, and the discharge temperature of the compressor T_{cpro} drop only slightly by 1°C. However, at the 64 minute, the accumulator is flooded and both the X_{ero} and $X_{acc,ro}$ drop significantly to 0.47 and 0.59. But the IHX can still prevent the compressor from being flooded. Though it shows the accumulator might be too small for the long operating time in the frosting.

3.2 Effects of different defrost-start criteria on frost accumulation

The mass of frost accumulation on the outdoor evaporator during the frosting process and after defrosting for 0°C and 90% RH are presented in Figure 6. To compare the effects of different defrost-start criteria, the final mass of frost is 0.42 kg for 5 times of the initial DP_{ea}, while it is 0.51 kg for 10 times of the initial DP_{ea}. Furthermore, the final mass of frost is the same for all continuous frosting processes with the same criteria. During the first frosting process of the longer operating time, the frost accumulates significantly faster in the first 40 minutes, at a speed of 15.0 g/s, and accumulates with a speed of 1.7 g/s in the next 24 minutes. Because the surface temperature increases as frost accumulate on the coil, and the accumulating speed decreases. Besides, the frost accumulates slower in the second frosting process: it starts with a speed of 11.1 g/s and then reduces to 2.3 g/s. The speed is decreased in the second frosting process due to the increased thermal resistance of the retained water film on the tubes and fins.

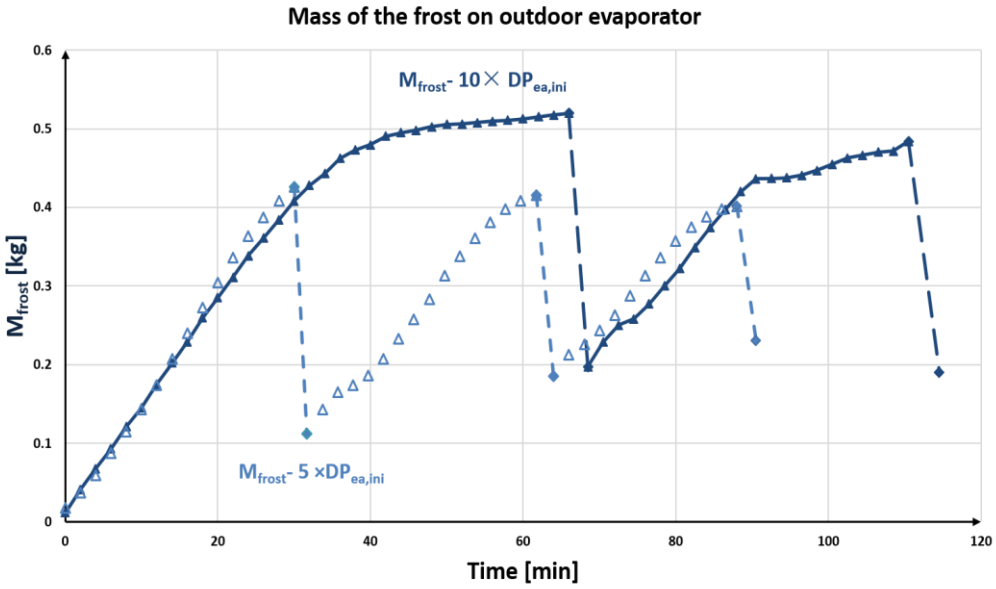

Figure 6: Comparison of M_{frost} with different defrost-start criteria for 0°C and 90% RH

As shown in Figure 6, it takes 1.7, 2.3, and 2.5 minutes to defrost for the continuous three defrosting processes with shorter frosting time, while it takes 2.5 and 4.0 minutes for the continuous two defrosting process with longer frosting time. All the defrost-stop criterion is the outdoor refrigerant exit temperature equals to 45°C. Overall, the percentages of defrosting time are 7.2% and 5.7% for 5 times and 10 times of the initial DP_{ea} as defrost-start criterion. This increased efficiency and heating time are at a cost of reduced heating capacity, and the user could be able to choose the defrost strategy for themselves.

Also, the masses of retained water after the defrosting process are 0.11, 0.19, and 0.23 kg for 5 times of the initial DP_{ea}, while 0.20 and 0.19 kg for 10 times of the initial DP_{ea}. Thus, the outdoor coil gets saturated after approximately three 30-minute frosting/defrosting cycles or a single 64-minute frosting process.

From the beginning to the 28th minute, outdoor air face velocity V_{eai} reduces from 3.12 to 1.97 m/s as DP_{ea} increases to 5 times the initial value. As shown in Figure 7-B, the frost accumulates mainly on the microchannel tubes and partially blocks the air-flow-channels between the louver fins and microchannel tubes. Especially, more frost accumulates on the surface of the second header and the inlet of the second pass. This is due to the lower surface temperature. Because of the sudden expansion of refrigerant from the MC tubes of the first pass to the second header, the local quality increases. Moreover, the intrusion of the microchannel tubes blocks the liquid from flowing towards the right. As a result, the local heat transfer coefficient increases and the surface temperature

reduces, and more frost accumulates. Also, as mentioned in the last section, X_{ero} drops from 0.90 to 0.72 at 28 minute, but the accumulator is not flooded yet and $X_{acc,ro}$ drops slightly from 0.87 to 0.86. Therefore, the cycle shifts little for the high-pressure side at the 28th minute.

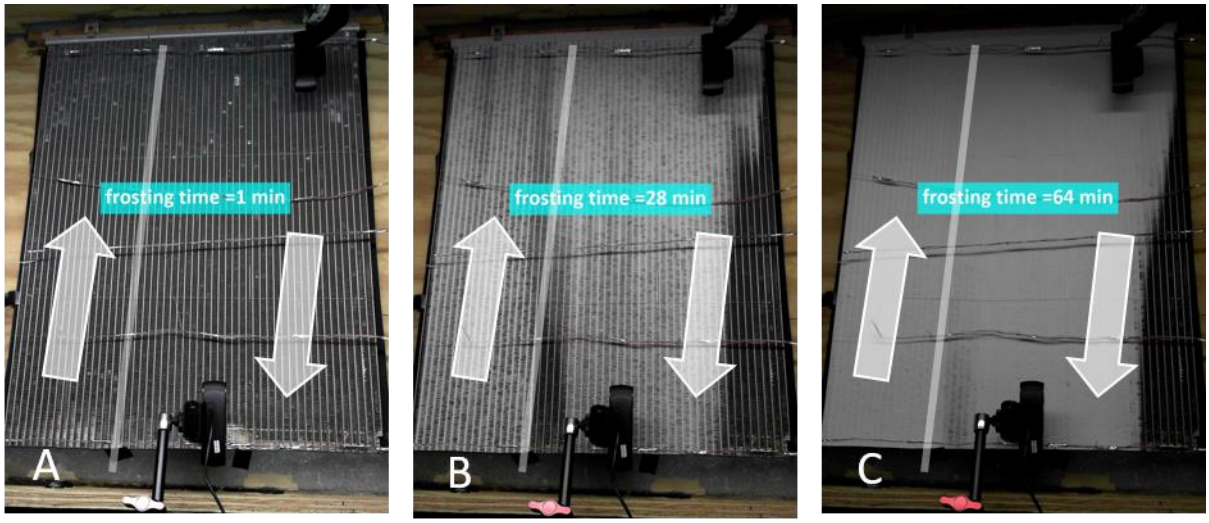

Figure 7: Frost distributions on the outdoor coil at 1, 28, and 64 minute of first frosting process for 0°C 90% RH

However, at the 64th minute, outdoor air face velocity V_{eai} reduces from 3.12 to 1.11 m/s as DP_{ea} increases to 10 times the initial value. Figure 7-C shows the frost distribution at 64 minute: almost the whole front surface is covered by solid frost, except a small triangle area at the right-bottom corner. Because of the mal-distribution, less liquid is flowing through the 7 tubes of the right side of the second pass. The superheated vapor in those tubes cannot absorb heat from the ambient air, and the heat transfer potentials of those areas are not utilized. Also, the quality X_{ero} drops from 0.90 to 0.47 at the 64 minute, and the accumulator is flooded as $X_{acc,ro}$ drops significantly from 0.87 to 0.59. The suction condition changes, and the high-side temperature and pressure decrease. The T-h plot shifts towards the left-bottom corner as shown by the purple dash line in Figure 5 and the temperature difference between T_{eai} and T_{ero} increases from 3 to 13°C.

4. CONCLUSIONS

A mobile CO_2 heat pump system was built, and a series of experiments were conducted to study the effects of different defrost-start criteria on the HP system efficiency and frost accumulation during periodic frosting/ defrosting processes. The results show:

- The HP system and capacity drops less than 10% with a defrost-start criterion of 5 times the initial DP_{ea}. The system can operate longer time during the frosting conditions by allowing a higher DP_{ea}.
- Refrigerant migrating into the accumulator is indicated by the fact that refrigerant qualities are different at the evaporator exit and accumulator exit. The evaporator exit quality X_{ero} is decreasing during each frosting condition, while the accumulator exit quality $X_{acc,ro}$ keeps constant until it is flooded.
- The operating time increases from 28 to 64 minutes for 0°C and 90% RH, when the defrost-start criterion changes from 5 to 10 times of the initial DP_{ea}. In the meanwhile, the defrosting time drops from 7.2% to 5.7%. This increased efficiency and heating time are at a cost of reduced heating capacity, and the user should be able to choose the defrost strategy for themselves.
- For the first frosting process in 0°C and 90% RH condition, the mass of frost accumulates on the outdoor coil at a speed of 15.0 g/s during the first 40 minutes and then reduces to 1.7 g/s, because the surface temperature increases as frost accumulate.
- For the retained water after defrosting processes, the outdoor coil becomes saturated after approximately three 30-minute frosting/defrosting cycles or a single 64-minute frosting process for 0°C and 90% RH.

NOMENCLATURE

AC	air-conditioning	**OCR**	oil circulating ratio [-]
Acc	accumulator	**P**	pressure [bar]
CO_2	carbon dioxide	**Q**	capacity [kW]
DP	differential pressure [Pa]	**T**	temperature [℃]
EXV	electronic expansion valve	**t**	time [s]
h	enthalpy [kJ/kg-℃]	**U**	mass flow rate [kg/min]
HP	heat pump	**V**	velocity [m/s]
HPF	heating performance factor	**W**	power [kW]
IHX	internal heat exchanger	**X**	quality [-]
M	mass [kg]	$\boldsymbol{\omega}$	humidity ratio [$kg/kg_{dry\ air}$]
$\dot{m}$	mass flow rate [kg/s]		

Subscript

a/ air	air-side	ini	initial
acc	accumulator	n	nozzle
c	gas cooler	o	outlet
cp/ comp	compressor	oi	oil inlet
dp	dew point	oo	oil outlet
e	evaporator	r/ ref	refrigerant-side
high	high-pressure side	x	expansion valve
i	inlet		

REFERENCES

Hayashi, Y., Aoki, A., Adachi, S., & Hori, K. (1977). Study of frost properties correlating with frost formation types. *Journal of Heat Transfer*, *99*(2), 239–245. https://doi.org/10.1115/1.3450675

Rahman, M. A., & Jacobi, A. M. (2014). Study of frost properties and frost melt water drainage on microgrooved brass surfaces in multiple frost/defrost/refrost cycles. *Applied Thermal Engineering*, *64*(1–2), 453–461. https://doi.org/10.1016/j.applthermaleng.2013.11.062

Robinson, C. M., & Jacobi, a M. (2001). *A Study of Frost Formation on a Plain Fin*. *61801*(217), 61. Air Conditioning and Refrigeration Center. College of Engineering. University of Illinois at Urbana-Champaign.

Steiner, A., & Rieberer, R. (2013). Parametric analysis of the defrosting process of a reversible heat pump system for electric vehicles. *Applied Thermal Engineering*, *61*(2), 393–400. https://doi.org/10.1016/j.applthermaleng.2013.07.044

Xia, Y., Zhong, Y., Hrnjak, P. S., & Jacobi, A. M. (2006). Frost, defrost, and refrost and its impact on the air-side thermal-hydraulic performance of louvered-fin, flat-tube heat exchangers. *International Journal of Refrigeration*, *29*(7), 1066–1079. https://doi.org/10.1016/j.ijrefrig.2006.03.005

Zhang, P., & Hrnjak, P. S. (2010). Air-side performance of a parallel-flow parallel-fin (PF2) heat exchanger in sequential frosting. *International Journal of Refrigeration*, *33*(6), 1118–1128. https://doi.org/10.1016/j.ijrefrig.2010.04.011

Zhang, W., & Hrnjak, P. (2020). Modeling of an Integrated Internal Heat Exchanger and Accumulator in R744 Mobile Air-Conditioning Applications. *SAE Technical Papers*, *2020-April*(April), 1–12. https://doi.org/10.4271/2020-01-0153

ACKNOWLEDGEMENT

This work was supported by Ford's University Research Project (URP) at the University of Illinois at Urbana-Champaign. All the help from Dr. Loren J Lohmeyer, Dr. Jing He, and Dr. Leyuan Yu are gratefully acknowledged!